Sign in

American Meteorological Society
AMS Journals Online

AMS Home | Journals Home | Journal Archive | Subscribe | For Authors | Help | Advanced Search | Search | Go

Full Text View

Volume 31, Issue 10 (October 2001)

Journal of Physical Oceanography
Article: pp. 3096–3120 | Abstract | PDF (777K)

Numerical Simulations of Buoyant Ekman Layers in the Presence of Variable Stratification. Part I: Constant Interior Forcing

A. Romanou and G. L. Weatherly

Department of Oceanography, The Florida State University, Tallahassee, Florida

(Manuscript received September 23, 1999, in final form April 24, 2001)

DOI: 10.1175/1520-0485(2001)031<3096:NSOBEL>2.0.CO;2

ABSTRACT

Two-dimensional numerical simulations of the turbulent buoyant Ekman layer in the presence of variable stratification help explain a transport mechanism for the detachment of the boundary layer flow around the front. Initially, a constant, spatially uniform, along-the-isobaths interior current and constant interior stratification are assumed. Buoyant inhibition of the boundary layer Ekman flow in the stratified region leads to shut down processes that are absent in the unstratified region. Depending on the direction of the interior flow, two dynamically distinct possibilities exist: (i) convergence around the front and subsequent export (*detrainment*) of boundary fluid toward the interior (southward forcing current, i.e., with shallow water on the right), and (ii) divergence around the front and subsequent import (*entrainment*) of interior fluid (northward interior forcing, i.e., with shallow water on the left or *y* positive). The position and strength of the convergence/divergence are controlled by the background diffusivity and the strength of the stratification. The area of detrainment (entrainment) represents a region of increased (decreased) bottom stress. In some of the studied cases, the bottom boundary layer on the unstratified region was modified by the presence of the front. An analogy between the case presented and the case of flow over variable topography is made.

Table of Contents:

Options:
- Create Reference
- Email this Article
- Add to MyArchive
- Search AMS Glossary

Search CrossRef for:
- Articles Citing This Article

Search Google Scholar for:
- A. Romanou
- G. L. Weatherly

1. Introduction

Various analytical and numerical studies over the last 25 years have been concerned with the evolution of the oceanic turbulent bottom boundary layers (BBL) over uniformly sloping bottom and in the presence of stable stratification. Such layers are often called buoyant Ekman layers (Weatherly and Martin 1978; Ezer and Weatherly 1990; McCready and Rhines 1991, 1993; Trowbridge and Lentz 1991; Middleton and Ramsden 1995, 1996). In all of the those studies, except that of Ezer and Weatherly (1990), only one-dimensional models with a constant slope or models with uniform stratification throughout the domain have been used. However, observations indicate that even though the one-dimensional treatment provides great insight, the description of the BBL is not complete, especially in areas of differential slope, like the continental shelf break, as well as at regions with changes in the stratification (fronts).

Observations suggest that the BBL on the upper continental slope is a region of high concentration of organic carbon and inorganic suspended matter and that the BBL may detach from the boundary at the shelf edge. Lin et al. (1992) described such distributions at approximately 700 m below the continental shelf break off the northeast coast of Taiwan. Walsh (1994) found similar patterns occurring at 500 m depth off the eastern U.S. coast at the Cape Hatteras slope, extending to very large distances in the interior. A transport mechanism that can explain such export of boundary layer flow from the shelf and into the interior, in the vicinity of a temperature front and/or a shelf break, is addressed here.

More recently, the shelfbreak and density fronts have received increasing interest and undergone more modeling effort. Lentz and Trowbridge (1991) pointed out the importance of using two-dimensional models for the study of the BBL where advective effects are fully taken into account, that is, not only in the advection of buoyancy by the cross-slope flow.

Gawarkiewicz and Chapman (1992) used a semispectral primitive equation model with constant eddy viscosity and diffusivity, no horizontal mixing, and a linear bottom stress condition to study the formation and evolution of shelfbreak fronts. For their choice of parameterization, the Ekman flow on the slope was quickly arrested, but little attention was given to the buoyant Ekman effects. The authors concluded that the density gradient across the shelf edge (due solely to the bottom topography) is responsible for the detachment of the BBL at the shelf break. Here, it will be shown that the spatial dependence of the boundary layer Ekman flow around the shelf edge due to the buoyant arrest of the flow on the slope is responsible for the observed shelfbreak effects. The adverse cross-shelf density gradients along the bottom are actually a transient consequence rather than the cause of the BBL detachment.

Chapman and Lentz (1994) studied numerically the formation and the evolution of a freshwater shelf front. In their results the buoyant Ekman layer dynamics is shown to eventually trap the freely moving front at a certain distance from the coast and establish upwelling/downwelling cells at each side of the front.

Houghton and Visbeck (1998) measured such a converging and upwelling situation at the vicinity of a shelfbreak front. They injected dye tracer into the BBL both above and below the front and measured the excursion in the interior of the dye patch. The present work agrees with their observations, expands on the idea of convergence and detrainment (to areas where the front may cause divergence and entrainment), and minimizes the number of requirements needed for convergence/divergence, that is, the shelf break and the front are each sufficient to produce such effects.

In particular, in the present work, the behavior of the turbulent boundary layer in the presence of a temperature front is explored in order to explain the features described by Lin et al. (1992) and Walsh (1994). A two-dimensional model with Mellor–Yamada closure schemes is used. Both the numerical procedure and the scheme were tested in the simple upwelling and downwelling Ekman layer cases on the continental slope. The model parameterization was chosen for comparison with the work of Weatherly and Martin (1978) and Middleton and Ramsden (1996) and significant agreement was achieved. An analogy between the case simulated and the case of a turbulent boundary layer over the continental shelf break (where the bottom slope varies) may be made.

In the following, a brief description of the formulation and the numerical procedure used is given. Results are shown for both the downwelling and the upwelling Ekman layer cases under steady interior forcing. The effect of increased interior mixing rates and greater stratification is also discussed.

2. Methodology

a. Model domain

In the study area (Fig. 1) the slope α is constant and the stratification is neutral in the upper half of the domain and uniform in the lower half. Close to the boundary, the isopycnals turn to intersect the bottom at right angles. The interior current is uniform in space and constant in time, flowing along the isobaths.

b. Governing equations

The momentum equations for a Boussinesq, rotating, and stratified ocean in a bottom embedded coordinate system and using the standard parameterization are

$$u_t + \mathbf{u}\cdot\nabla u - fv = -p_x + g\beta\alpha(T - \overline{T}) + (A^x u_x)_x + (A^z u_z)_z \qquad (1a)$$

$$v_t + \mathbf{u}\cdot\nabla v + fu = -p_y + (A^x v_x)_x + (A^z v_z)_z, \qquad (1b)$$

where the x axis points downslope and across the isobaths and $x = 0$ at the front and the z axis is perpendicular to the boundary. The bottom slope α is assumed small enough so that $\sin\alpha \approx \alpha$, $\cos\alpha \approx 1$. Only terms greater or equal to $O(\alpha)$ are maintained, $p_y = 0$, the interior velocity $V_g = p_x/(\rho f)$ is uniform and constant and so is $\overline{T}$, the temperature field in the absence of BBL. A linear equation of state is assumed; that is, the density variations result from temperature changes only and $\rho = (1 - \beta T)$ where β is the thermal expansion coefficient.

The continuity and density equations maintain their form in the new coordinate system:

$$T_t + uT_x + wT_z = (K^x T_x)_x + (K^z T_z)_z \tag{1c}$$

$$u_x + w_z = 0, \tag{1d}$$

where K^{xz} are the thermal diffusivities.

c. Boundary and initial conditions

To close the problem, the following boundary conditions need to be employed. At the bottom $z = 0$, no slip condition:

$$u = v = 0, \tag{2a}$$

insulated bottom:

$$T_z = 0, \tag{2b}$$

that is, no heat flux through the bottom.

At the top of the domain, well outside the bottom boundary layer,

$$p_x = fV_g \tag{2c}$$

$$p_y = 0 \tag{2d}$$

$$T_z = 0. \tag{2e}$$

The top boundary is taken to be thermally insulated and the side boundaries are considered to perfectly conduct momentum and heat.

To reduce the effect of the inertial oscillations, present in the first few days of the simulations, p_x is increased linearly to its constant value over a period of one day.

d. Parameters and scaling

The interior current $(U_g, V_g) = (0, \pm 15)$ cm s^{-1} is assumed constant and along the isobaths. The background stratification, $\overline{T}_z = 7 \times 10^{-4}$°C/cm, and the interior Brunt–Väisälä frequency, $N = 1.28 \times 10^{-2}$ s^{-1}, are also constant everywhere in the interior and as depicted in Fig. 1. The slope is $\alpha = 2.4 \times 10^{-3}$, and the thermal expansion coefficient is $\beta = 2.4 \times 10^{-4}$°C^{-1}. The Coriolis parameter is constant, $f = 6.3 \times 10^{-5}$ s^{-1}, and therefore the north (south) direction in the following relates to positive (negative) y [or flow with shallow water on the left (right)]. The background vertical eddy viscosity and the eddy diffusivity are $A^z_0 = 10^{-2}$ cm^2 s^{-1} and $K^z_0 = 10^{-3}$ cm^2 s^{-1}, respectively. The parameterization is chosen to facilitate comparison with Weatherly and Martin (1978) and Middleton and Ramsden (1996).

An important parameter for the stratified region is the McCready–Rhines timescale:

$$\tau_0 = f/(N\alpha)^2. \tag{3}$$

As discussed in McCready and Rhines (1991), τ_0 is the time it takes for the buoyancy term in Eq. (1a) to become important.

For the problem considered here, $\tau_0 = 18.5$ h; therefore, the tendency terms in Eqs. (1a–c) must be taken into account at all times. The Rossby number associated with the interior flow is $O(1)$ or larger if the horizontal length scales are $L \lesssim 2.4$ km. Since a priori the width of the region affected by the front is unknown, the nonlinear terms will be retained in the model simulations. Later, it will be seen that the transition region from the neutral to the stratified region is $O(10$ km$)$ wide and the nonlinear terms are negligible in the equations of motion.

3. The numerical model

The model used in the following simulations is a two-dimensional primitive equation Sandia Ocean Modeling System (SOMS-3D), developed by Dietrich et al. (1987; Dietrich 1993). In the domain modeled (Fig. 1), the slope of the boundary is constant and only half of the domain is assumed to be stratified. In the lower half ($x > 0$), the buoyancy force, $g\beta\alpha(T - \overline{T})$, is important. The upper half ($x < 0$) is not stratified and the buoyancy term there is zero. An initial mixed layer of 5-m height is assumed across the whole boundary. Above the neutral region, a steplike temperature jump at $z = 5$ m is assumed so as to limit the BBL thickening there. Basically the boundary layer in that region is like the BBL over a level bottom formed in a mixed layer capped by a temperature jump (Weatherly and Martin 1978).

a. The domain

The dimensions of the domain are $L^X = 160$ km, $H = 100$ m, and the grid spacing is $\delta x = 2$ km. The bottom is assumed hydrodynamically rough and the roughness length scale z_0 [see Eq. (7)] is taken to be constant, $z_0 = 3 \times 10^{-2}$ cm. The vertical grid is stretched, logarithmic close to the bottom and linear in the interior. There are four levels within the first 5 m while in the interior $dz \approx 3$ m. The time step, $\delta t = 20$ min, is chosen to satisfy the Courant stability criterion $C\ \delta t/\delta x \ll 1$, where C is the speed of the fastest moving internal wave.

b. Horizontal diffusion

The horizontal diffusivities (A, K) are modeled according to Yamada (1979):

$$(A, K)^X = (A_0, K_0)^X + c_1(\delta x)(\delta y)|(u, T)_x|, \quad (4)$$

where $(A_0, K_0)^X$ are the interior (background) values for the horizontal diffusion of momentum and heat =(0.1, 0.05) cm^2 s^{-1}. The coefficient c_1 is taken 0.02 for the stretching terms [i.e., when the stress is applied in the direction of the shear, as for the calculation of $(u_x)_x$] and 0.01 for the straining terms [i.e., for the stress perpendicular to the shear, like $(u_y)_y$]; c_1 can be adjusted to minimize the computational noise. The values ascribed to c_1 here are the ones suggested in Yamada (1979) and Dietrich et al. (1987).

c. Vertical diffusion and turbulence closure scheme

The Mellor–Yamada 2½ order turbulence closure scheme is used for the calculation of the vertical eddy viscosity and diffusivity. The turbulent kinetic energy equation is solved

$$E_t + uE_x + wE_z = (A^x E_x)_x + (K_E E_z)_z + A^z(u_z^2 + v_z^2) - K_H^z g\beta(T - \alpha\overline{T})_z - \frac{q^3}{Cl}, \qquad (5)$$

(Click the equation graphic to enlarge/reduce size)

where

E the TKE density $= \dfrac{q^2}{2} = \dfrac{1}{2}(\overline{u'^2} + \overline{v'^2} + \overline{w'^2})$,

l the turbulent eddy length scale $= \kappa z \Big/ \left(1 + \dfrac{\kappa z}{l_0}\right)$,

κ 0.4 is the von Kármán constant,

l_0 the maximum turbulent length scale $= \gamma \displaystyle\int_0^{H_T} zq\, dz \Big/ \int_0^{H_T} q\, dz$,

γ 0.2,

K_E is the coefficient for the diffusion of TKE, and $C = 16.6$. [Note that Weatherly and Martin (1978) and Middleton and Ramsden (1996) took $\gamma = 0.3$, so the results presented here will be qualitatively similar but quantitatively different from theirs.]

The vertical eddy viscosity A^z, eddy diffusivity K^z, and the kinetic energy diffusivity K_E are subsequently defined as in the Mellor–Yamada scheme (1982):

$$A^z = A_0^z + lqS_M \qquad (6a)$$

$$K^z = K_0^z + lqS_H \qquad (6b)$$

$$K_E = K_{E0}^z + 0.2ql, \qquad (6c)$$

where A^z_0, K^z_0, and K^z_{E0} are the background (interior) diffusivities, and S_M and S_H are functions of the vertical shear in the velocity

$$\frac{l^2}{q^2}(u_z^2 + v_z^2)$$

and the vertical gradient in the temperature field

$$\frac{l^2}{q^2}T_z$$

(see also Ezer and Weatherly 1990).

d. Boundary conditions

To ensure the no-slip boundary condition at the bottom, the logarithmic law-of-the-wall is applied at the lowest vertical grid levels:

$$u(z) = \frac{u_*}{\kappa}\ln\left(\frac{z}{z_0}\right), \qquad (7)$$

where the friction velocity $u_* = q/B^{1/3}_1$ and $B_1 = 16.6$. The vertical velocity, calculated through the incompressibility equation, is set to zero at the bottom.

e. Convective adjustment scheme

The numerical solution may develop gravitational (static) instabilities in the form of unstable temperature vertical profiles. Many procedures have been proposed in the literature for restoring the static stability of the water column in areas where it has been underestimated by the numerical model (Killworth 1989; Marotzke 1991; Yin and Sarachik 1994).

To eliminate the static instabilities, the Mellor–Yamada scheme has been implemented with a convective adjustment scheme that instantaneously (i.e., at each time step) mixes any unstable regions. The adjustment is carried out explicitly, using an iterative method with a “tolerance” margin $O(10^{-5})$ in grad °C/cm. Major emphasis is given to the thermal energy conservation during the calculations since this would also affect the height of the mixed layer across the boundary.

This scheme is similar to the complete adjustment schemes proposed by Marotzke (Marotzke 1991) and Yin and Sarachik (Yin and Sarachik 1994) for the large-scale ocean general circulation models.

4. Results

a. Downwelling Ekman layers near a temperature front

1) LOW BACKGROUND DIFFUSION

In the neutral region, the along-isobaths interior current imposes an Ekman flow across the depth contours and downslope ($f > 0$). There is no other stratification effect except the temperature jump in order to limit the BBL thickness there (Fig. 2a). The across-slope component of the flow u has a jetlike signature (Fig. 2e), while the alongslope component decays quickly from its geostrophic value V_g (Fig. 2i).

In the stratified region, buoyancy effects become important after time $t \approx \tau_0 = 18.5$ h, through the advection of the background buoyancy field. The cross-slope velocity u transports water across the isopycnals, altering locally the temperature field. This change imposes a buoyancy acceleration, $g\beta\alpha(T - \overline{T})$, of increasing magnitude that opposes the Ekman flow (*inhibited Ekman flow*). The buoyancy fluxes, bringing warmer water under cold, destroy the thermal stability of the water column, leading to convective overturning, and the turbulent mixing is enhanced. The mixed layer height grows at a decreasing rate (Fig. 2d), and the cross-slope velocity is reduced to half that far upslope and continues to decrease slowly (Fig. 2h). The alongslope velocity is linear with depth except near the bottom (Fig. 2l). The *shut-down* state (when the Ekman flow is essentially reduced to zero) is achieved when the thermal wind balance; that is, the buoyancy acceleration,

$$g\beta\alpha(T - \overline{T}),$$

is large enough to balance the Coriolis acceleration, $f(\upsilon - V_g)$, throughout the BBL. The vertical stress term $(A^z u_z)_z$ is then negligible. The model results show a shut down time of approximately 5 days, which agrees well with other estimates (Weatherly and Martin 1978; Trowbridge and Lentz 1991; McCready and Rhines 1993; Middleton and Ramsden 1996).

Inertial oscillations, with timescale

$$T_{\text{inertial}} = \frac{2\pi}{f(1 + \alpha^2 N^2/f^2)^{1/2}}, \qquad (8)$$

approximately 25 h (Weatherly 1978), are important during the first few time steps (Figs. 2e,f,g,h). They result in a net advection of fluid parcels both along and across the isobaths. For example, above the BBL, they result in a net positive cross-slope displacement of the front of almost 2 km. Most of this displacement occurs during the first inertial period. Therefore, in the following, the front will be considered at $x = 2$ km.

As the flow on the shelf approaches the front, the BBL [unlike the bottom mixed layer (BML)] gets thicker (Fig. 2b), the cross-slope velocity gets slightly reduced (Fig. 2f), but the alongslope flow remains almost the same (Fig. 2j). Immediately below the front, the BBL height increases, the cross-slope flow is faster than that farther downslope (Fig. 2g), and the alongslope flow resembles the one in the neutral region (Fig. 2k). Therefore, the front affects a wide region around it.

The ensuing variability of u results in areas of convergence and divergence at the front. In particular, since the flow above the front changes little with time and the flow in the stratified region decreases with time due to the buoyancy effects, convergence around the front will occur and subsequently impose vertical motion towards the interior, as described by the continuity equation (1d). Since $w_z = 0$ in the interior and $w(\text{bottom}) = 0$, any vertical velocities created at the BBL will be communicated to the whole water column (Fig. 3) within a “detrainment zone.” The width of this zone is 15 km after 10 days and its axis is situated before the front at $x = 2$ km. The detachment of the boundary layer flow has been observed at downwelling fronts by Weatherly and Kelley (1985) and has been studied numerically by Ezer and Weatherly (1990), Gawarkiewicz and Chapman (1992), and Chapman and Lentz (1994). In Ezer and Weatherly (1990), the front associated with a cold filament at the continental rise was shown to change differently upslope than downslope, due to buoyant Ekman layer dynamics. In Chapman and Lentz (1994), the front developed as a freshwater inflow entered and flowed along the shelf and spanned the whole water depth. From their input values, the shutdown time is O(11 days) and much greater than here, thus inhibiting the downslope translation of the front after 120 days.

A zone of negative velocities perpendicular to the boundary is observed to the right of the detrainment region (Fig. 3). This “entrainment zone” is the result of the cross-slope gradient of the transverse (u positive) circulation that occurs between 8 and 15 m above the bottom in the stratified region, as a comparison of Figs. 2g and 2h shows. The u flow below the front is upslope and stronger than the one in the lower half so that the upwelling circulation diverges entraining water from the interior.

The dual appearance of detraining and entraining regions is also reported by Gawarkiewicz and Chapman (1992), who attributed the detrainment only to the cross-slope density gradients close to the front, a sole effect of the change of the bottom slope. Another reason is proposed here. Buoyant arrest of the BBL Ekman flow on the stratified part of the slope causes the convergence around the front. Detrainment of BBL fluid follows and the deformation of the front is the result of the detachment rather than the cause of it. This is also reported in Chapman and Lentz (1994).

The vertical velocities created from the convergence around the front advectively drive boundary fluid toward the interior, distorting the shape of the isotherms. To visualize such effects, a passive tracer is ejected inside the BBL of the neutrally stratified region (Fig. 4) with homogeneous tracer concentration. Processes inside the mixed layer will change the concentration distribution in time. Advection of the tracer both downslope (due to the Ekman flow) and perpendicular to the bottom (due to the thickening of the BBL) dilutes the initial tracer concentration. Most of this change occurs during the first inertial period but continues at a decreased rate after that. After 10 days, tracer has reached 40 m above the bottom immediately before the front and 15 m above the bottom farther upslope. At the same time, tracer has entered the upper stratified region (15 km). The reduced Ekman flow there cannot further advect the tracer. The front, therefore, acts as a very effective barrier, diverting most of the tracer into the interior and not far downslope.

Another consequence of the vertical shear in the velocity fields is the appearance of a region of pronounced mixing near the front. In the vicinity of the front and below it, homogenization of the temperature inside the BBL decreases the mixing significantly. However, before the front the thermocline in the upper BBL (Fig. 2b) in conjunction with the shear there (Fig. 2f) initiate large convective mixing (Fig. 5).

The bottom stress (divided by the reference density ρ_0), is computed by the vertical integral of the momentum equations. It is therefore the total stress with components

$$\tau^y = -\int_{\mathrm{bot}}^{\mathrm{top}} \left(\frac{dv}{dt} + fu \right) dz, \qquad (9b)$$

so that $\tau^b = (\tau^2_x + \tau^2_y)^{1/2}$, where d/dt is the total derivative.

The bottom stress (Fig. 6) increases rapidly during the first day of calculations due to inertial oscillations. Initially, in the unstratified region the stress is 0.35 cm^2 s^{-2} but after a few inertial cycles it decreases to 0.12 cm^2 s^{-2}.

In the stratified region, the buoyancy force increasingly tends to balance the Coriolis and the pressure forces, reducing the cross-slope stress component τ^x, in agreement with Middleton and Ramsden (1996). After 10 days the cross-slope component of the bottom stress is 0.025 cm^2 s^{-2}. The total stress on the lower part of the slope is decreasing with time and after 10 days it is 0.03 cm^2 s^{-2}. Its spatial variation (Fig. 6) covers approximately 25 km around the front. To the left of the front, the stress does not change with time, whereas to the right, it decreases due to the shut-down process. Immediately above the front, the stress at day 10 is significantly reduced because the cross-slope velocity (and subsequently τ^y) decreases there. Below the front, at $x = 8$ km, τ^b is maximum because the cross-slope component τ^x increases to its maximum value there. The buoyancy force grows larger than the Coriolis and pressure forces since the vertical advection of colder fluid increases the temperature contrast at the top of the BBL (Fig. 4). Therefore, the stress before the front is dominated by the alongslope component, while below the front by the cross-slope component.

The horizontal diffusivities are found to be between 10^{-1} and 10^5 cm^2 s^{-1} with the maximum occurring at the front and inside the BBL. In the subsequent simulations these values did not change much.

Consistent with the scaling of equations (Romanou 1999), the nonlinear terms are found small throughout the domain. As shown in Figs. 3, 4, 5, and 6, the width of the region where the “frontal” dynamics (convergence and detrainment) take place is approximately 10 km, a cross-slope scale that ensures that the Rossby number is always less than 1.

2) HIGH BACKGROUND DIFFUSION

The magnitude of the vertical (turbulent) diffusivity in the interior and deep ocean has been discussed by many researchers. Munk (1966) and Hogg et al. (1982) suggested a value for the interior thermal diffusivity of the order of 1 cm^2 s^{-1} while Gregg (1989) suggested values of the order of 0.1 cm^2 s^{-1}. Microstructure measurements by Polzin et al. (1997) showed that diapycnal diffusivities are of the order of 0.1 cm^2 s^{-1} in most of the Brazil Basin interior, above smooth abyssal plains and the continental rise. A fivefold increase of this value is found above rough topography such as the Mid-Atlantic Ridge.

The sensitivity of the buoyant Ekman layer processes to the vertical background (interior) diffusivities has also been commented by various authors (McCready and Rhines 1991; Middleton and Ramsden 1996). In particular Middleton and Ramsden (1996) found that increasing the background diffusivities from their molecular values to 1 cm^2 s^{-1} invariably affected their results. In the downwelling simulations, the arrest of the buoyant BBL was faster, although no physical reason was presented. A justification is given below as it helps in interpreting the changes seen across the slope at both sides of the front.

Upslope, where the BBL is not a buoyant one, the results of the last section give $\tau^b = 0.12$ cm^2 s^{-1}, where τ^b is the bottom stress per unit density. If $\tau^b = C_D V_g$, then the drag coefficient $C_D = 0.008$ cm s^{-1}. Standard Ekman theory gives $C_D = (A^z_0 f)^{1/2}$. With $A^z_0 = 0.01$ cm^2 s^{-1}, $C_D = 0.001$ cm s^{-1}, while with $A^z_0 = 1$ cm^2 s^{-1}, $C_D = 0.008$ cm s^{-1}. Thus, with low background diffusivity most of the bottom stress (i.e., the Ekman transport) is due to BBL generated turbulence, while for the high background diffusivity most of it is due to the background diffusivity itself. Therefore, it is not surprising that Middleton and Ramsden (1996) and others found that buoyant BBL processes over sloping bottoms were sensitive to whether the background diffusivity was low (molecular) or high (turbulent) = 1 cm^2 s^{-1}.

Analogous simulations of the boundary layer as in section 4a(1) (hereafter referred to as “standard case”) are carried out here assuming a more diffusive interior. Both eddy coefficients are increased, that is, $A^z_0 = 1$ cm^2 s^{-1} and $K^z_0 = 1$ cm^2 s^{-1}. Good agreement with the Middleton and Ramsden (1996) results is achieved for the lower (stratified) part of the domain.

The inertial oscillations are again strong, especially during the first day of calculations. The net displacement of the front is 2 km downslope.

The shutdown timescale is again 18.5 h. However, the shutdown time is less than in the standard case because the Ekman flow downslope is reduced faster than in the low diffusion case.

With a more diffusive interior the cross-slope velocities in the BBL upslope are about 40% larger, mixing extends deeper in the interior, and the cross-slope velocity profiles exhibit less vertical shear at the top of the BBL (Fig. 7e and Fig. 2e). These effects are the result of increased bottom stress in the BBL (increased Ekman transport) when the interior diffusivity is increased. The mixed layer exhibits a multilayer form (Fig. 7a) and the alongslope velocity below the front (Fig. 7i) is not linear with z. Upslope, the flow decreases as it approaches the front (Fig. 7f), and after the front, the flow decreases as it enters the slope region (Fig. 7g); that is, the spatial variability is similar to the standard case.

The upslope flow is stronger and combined with the slightly arrested flow in the stratified region leads to a more intense convergence around the front. Indeed, Fig. 8 shows that the current upslope is stronger and the BBL there is thicker, but below the front the current is almost the same as in the standard case. The strength of the detrainment zone is therefore increased. Its width, ~ 12 km, is slightly less than in the previous case and its axis is situated 2 km to the right of the front. Therefore, the position and the width of that zone are only slightly affected by the strong background diffusion.

Further, there is no divergence zone, which before was attributed to the cross-slope variation of u and the vertical shear that develops at the top of the BBL below the front region. High background diffusion stabilizes the cross-slope flow above the BBL and removes the inflection points from the vertical profiles.

Results also obtained in this simulation (not shown here; Romanou 1999) indicate that high interior diffusivity results also in (i) BBL detrainment into the interior that extends to 60 m above the bottom (i.e., much farther than in the standard case), and (ii) intensive mixing that occurs again at immediately before the front, as in the standard case.

3) STEEPER BOTTOM TOPOGRAPHY

The bottom inclination controls the flow above the slope and, when coupled with stratification, it imposes a buoyancy force that acts to decrease the Ekman flow. A bottom slope three times as large as in the standard case [section 4a(1)] is considered here; that is, $\alpha = -7.2 \times 10^{-3}$, for a more realistic representation of the slope topography.

Increasing the absolute value of the slope α in Eq. (1a), increases the buoyancy force $g\beta\alpha(T - \overline{T})$ and accelerates the shut-down processes. Indeed, a three-fold increase in the bottom slope results in a one-ninth-fold decrease in the shut-down timescale, $\tau_0 = f/(N\alpha)^2 = 2$ h. The model predicts successfully the tendency to shut down faster on the slope (Fig. 9h). The mixed layer above the stratified region initially has a small vertical structure that quickly disappears (Fig. 9d). The flow close to the boundary is reduced greatly and there is significant downslope flow between 5 and 10 m above the bottom, which also decreases with time. Then, the boundary layer restratifies. The net displacement (2 km downslope) of the front due to the inertial oscillations is again shown to occur mostly during the first day.

To the left of the front, the mixed layer height is greater than in the standard case (Fig. 9b), reaching 38 m below the front (which is at $x = 2$ km) and 40 m right at the front by day 10. Farther downslope, it quickly settles to the values of the stratified case (Fig. 9c).

The cross-slope velocity below the front (Fig. 9g) reverses sign and upwelling is enhanced. This effect is very restricted spatially and occurs within 2 km. The profiles everywhere around the front exhibit significant vertical structure. Finally, both the along- and the across-slope velocity fields resemble the slope dynamics in the vicinity of the front; that is, the region affected by the front is narrower.

Increasing the bottom inclination shuts down the flow in the stratified region faster but has essentially no effect on the flow in the neutrally stratified region. Therefore, the cross-slope velocity gradient around the front is enhanced, resulting in more pronounced vertical velocities in the detrainment zone. Comparison of Figs. 10 and 3 shows a twofold increase in the strength of this zone. That the velocity at the front quickly obtains the slope-flow characteristics effects a thinner detrainment zone, which is thus located closer to the front. After 10 days, it is situated almost 2 km below the initial front and its width is 6 km. The BBL flow, experiencing quickly the shut-down effects there, leaves the boundary sooner and faster.

The tracer and temperature sections across the boundary confirm this conclusion (Romanou 1999). By the end of the experiment (after 10 days), tracer is ejected to 80 m above the boundary. The maximum mixed layer height at day 10 is 38 m and is located very close to the shelf edge (as opposed to 8 km below it, in the standard case). The steeper slope further prevents the penetration of the "neutral" BBL into the "stratified" BBL. Instead, it directs it more effectively toward the interior, as is also shown in Fig. 10.

Turbulent mixing and turbulent kinetic energy sections (shown in Romanou 1999) in the neutrally stratified region have essentially the same values as before. Downslope, the Richardson criterion suggests that during shutdown, turbulence is extinguished (Ri = 0.47). Indeed, the mixed layer on the slope is found to restratify, the Richardson number increases, and turbulence is progressively extinguished. Moreover, above the stratified region the values of the eddy diffusivity decrease significantly with time and by day 10, the maximum eddy diffusivity is 0.4 $\mathrm{cm}^2\ \mathrm{s}^{-1}$ (as opposed to the standard case where the maximum eddy diffusivity at day 10 was 4 $\mathrm{cm}^2\ \mathrm{s}^{-1}$).

Further, turbulent mixing is expected to be increased around the front within a narrower region because the shear in the cross-slope velocity is more pronounced and more confined spatially. Intensive mixing occurs again to the left of the front and at the same positions as in the standard case.

The bottom stress is upslope the same as in the standard case (0.12 cm^2 s^{-2}), and less, downslope (0.02 cm^2 s^{-2} at day 10). The fast shut down is responsible for the stress reduction on the slope. Restratification of the mixed layer inhibits turbulent mixing and the overall effect is complete shut down of τ^y as well. Around the front, the bottom stress is three times as large as before. To the left of the front, at $x = 2$ km, it obtains its maximum value of 0.64 cm^2 s^{-2} and at $x = 4$ km it is 0.33 cm^2 s^{-2}.

b. Upwelling Ekman layers around a temperature front

1) LOW BACKGROUND DIFFUSION

Similar to the downwelling Ekman layer case discussed in the previous section, an upwelling Ekman flow with a weakly diffusive interior will be addressed next.

Reversing the direction of the interior geostrophic current V_g (Fig. 1) results in an upslope Ekman transport, imposed by the balance between the geostrophic and frictional forces. Colder (less buoyant) water is now advected upslope, the temperature difference between the mixed layer and the interior increases, that is, the Richardson number increases, and the static stability of the water column is enhanced. Turbulent mixing that sustains the mixed layer is thus inhibited. The possibility that advection of denser water under lighter in the presence of turbulent boundary mixing, which creates very thin bottom layers, has been suggested before (Weartherly and Martin 1978; Trowbridge and Lentz 1991; Garrett et al. 1993; Middleton and Ramsden 1996).

The upwelling regions therefore are regions of very restricted mixing and thinner mixed layers as opposed to the downwelling regions that represent regions of significant mixing and thicker mixed layers (Weatherly and Martin 1978; Lentz and Trowbridge 1991). One important feature of buoyant Ekman layers is their *asymmetric* response under change in the direction of the buoyancy forces. In the upwelling case, the shut-down time is reduced, the mixed layer is thinner, and the thermal wind shear above the BBL is time dependent. The asymmetry between the upwelling- and the downwelling-favorable responses to the interior forcing and the background stratification has been pointed out previously [Weatherly and Martin (1978); Trowbridge and Lentz (1991)] and is consistently found here.

The cross-isobath velocity is quickly reduced in the stratified region (Fig. 11h), indicating that the shutdown of the Ekman flow occurs faster than in the downwelling-favorable case, in agreement with Middleton and Ramsden (1996) and Trowbridge and Lentz (1991). The along-isobath velocity field in the same region indicates that in an upwelling Ekman layer the thermal wind balance has a different form (Fig. 11l). Vertical differentiation and linearization of Eq. (1b) at shut down gives

$$v_z = \frac{\alpha}{f}(N^2 - g\beta T_z). \qquad (10)$$

In the upwelling-favorable case, above the thin mixed layer but inside the boundary layer, the temperature stratification is greater than the interior stratification (Fig. 11d) and must be taken into account. In the downwelling Ekman case, the second term in Eq. (10) was zero.

The shut-down time must be less than in the downwelling case (less than 5 days) because the BBL height is smaller and the Ekman flow is the same. The buoyancy forces are distributed over smaller height, thus becoming more effective in opposing the Ekman flow. The model predicts a shut down time of 2 days, in good agreement with other estimates (McCready and Rhines 1993; Garrett et al. 1993; Middleton and Ramsden 1996).

Finally, inertial oscillations are present in this case as well. Their timescale [Eq. (8)] and amplitude are independent of the Ekman flow direction. However, their effect around the front is found to be more pronounced here. The front is shifted by 6 km upslope (in the neutrally stratified region), mostly during the first day. In the stratified region and in the interior, this net “inertial shift” is approximately 2 km. The difference should be attributed to the fact that the flow on the shelf is faster and pushes the front farther onto the shelf. In the following, the new position of the front as it is adjusted by the inertial oscillations will be taken at $x = -2$ km.

To the left of the front, the BML height is 1.5 m at day 2 and remains the same for the rest of the calculations (Fig. 11b). The cross- and the alongslope velocity fields (Figs. 11f,j) resemble more the buoyant, Ekman layer characteristics. This is an indication that increasingly arrested Ekman flow from down the slope, moving while upwelling, enters the unstratified region. Therefore, some buoyant Ekman layer dynamics “enter” the region upslope and influence a continuously wider region there, in contrast with the downwelling case where the front and the shut down on the lower slope prevented the upslope dynamics from entering the lower slope region.

Below the front, the mixed layer height also extends to 1.5 m above the bottom and appears to warm up after 4 days (Fig. 11c). Warming of the mixed layer occurs also upslope in the vicinity the front. Since the u profiles do not indicate any downslope flow that could advectively bring warmer water, this warming is attributed to diffusive fluxes from the interior and entrainment of overlying warmer water. After the BML height collapses to 1.5 m due to the buoyancy fluxes from the lower slope, mixing inside this layer is maintained. Moreover, different positions upslope experience this effect with a time lag because stratified water that flows upslope progresses farther and restratifies the bottom layer, which is then remixed by diffusion.

The divergence of the velocity field around the front imposes downwelling vertical velocities from the interior and "pumping" (entrainment) of the interior fluid downward into the BBL (Fig. 12). The flow to the left of the front speeds up because of the intruding buoyant Ekman downslope flow discussed earlier. The divergence moves along with the intruding flow upslope and occurs in a wider region than the detrainment zone in section 4a(1). Therefore, the entrainment is weaker and not as clearly defined as the detrainment zone. The entrainment zone is situated below the front (which is at $x = -2$ km) and extends to 25 km to the left and 4 km to the right of the front. The cross-slope flow at the top of the boundary layer (at 5–10 m) is downwelling. Weak convergence occurs below the front (Fig. 12) due to the vertical structure of the cross-slope velocities there.

In Fig. 13, the isotherms decline towards the bottom within 30 km before the front. By day 4, the frontal isotherm has reached the minimum height of 2 m above the bottom, which is maintained for the rest of the model run. At the same time, the entrainment widens upslope as more stratified water is transported to the left of the front. Detrainment of BBL fluid toward the interior occurs again at $x = 8$ km below the front and at $x = -10$ km above it (Fig. 13).

By the tenth day, tracer from the slope has reached 22 km upslope. As shutdown occurs downslope, less tracer escapes toward that region. Tracer is continuously advected upslope and diluted by background diffusion. Therefore, the asymmetrical behavior of the buoyant Ekman flow is extended to the region of the front; the upwelling front acts to both advect vertically into the interior BBL fluid but also to transport it farther upslope. The effect of the front is obvious over a wider region than in the downwelling case.

As expected, turbulent mixing and turbulent kinetic energy production on the upper slope are the same as in section 4a(1) because the upwelling and downwelling Ekman flows there are symmetrical (Fig. 14). On the lower slope, turbulence is decreased significantly. By the end of the run, the maximum eddy diffusivity has dropped to molecular values.

Progressively, the left side of the front becomes less turbulent, another indication that some nearly shutdown flow from the lower slope ascends to the region left of the front. In fact, this property can identify upwelling fronts in the real ocean; to the left of the front there is much less turbulence. A maximum-mixing region appears again there in the beginning and then moves farther upslope with the intruding flow.

The bottom stress (Fig. 15) is 0.12 $\text{cm}^2\ \text{s}^{-2}$ upslope, the same as for the case in section 4a(1). Downslope it is reduced to zero at day 10, indicating a fully arrested Ekman flow. Around the front, the stress initially decreases because it experiences the shutdown effects either directly (from downslope) or through the intrusion of stratified water (upslope of the front). As time progresses, the stress increases and finally becomes more vigorous than the stress on the shelf. After 5 days, there is significant stress reduction before the front (at $x = -2$ km) and the width of this "low-stress" region is 15 km. After 10 days, the stress is further reduced in a wider region (25 km). The reduction of the stress before the front is attributed mainly to the reduction of τ^y and the cross-slope velocity u. Below the front the stress increases abruptly to its maximum value (0.22 $\text{cm}^2\ \text{s}^{-2}$) and then drops to its minimum value on the slope. The width of the "high-stress" region is unchanged, but the maximum is shifted closer towards the front at day 10. Similar to the downwelling case, the stress increase below the front is attributed to the strong buoyancy force at the site of detrainment toward the interior.

2) HIGH BACKGROUND DIFFUSION

When the background eddy viscosity and diffusivity are increased to 1 $\text{cm}^2\ \text{s}^{-1}$, the upwelling of colder water downslope occurs within a thin mixed layer, its thickness predicted by $\sim (2A^{z^2}{}_0/f\,)^{1/2} = 2$ m and maintained even after 10 days, unlike in the standard upwelling case where the upwelling was eventually arrested and the mixed layer was negligibly thin.

That the intrusion of cold, stratified water to the left of the front, is present but not as pronounced is also seen in Figs. 16f,j. The profiles of the cross-slope velocity at $x = -4$ km differ little from those upslope, but together with the alongslope velocity profiles, they indicate the presence of shutdown effects. The BML height is 4 m (Fig. 16b) and its temperature decreases with time as fast as downslope. Below the front (Figs. 16c,g,k), the velocity profiles are comparable to the ones upslope. The mixed layer is very thin (1.5 m) but the cooling rate there is almost twice than that downslope.

The divergence of the cross-slope velocity around the front leads to entrainment of interior fluid into the BBL (Fig. 17). As in section 4b(2), the cross-slope velocity is stronger and the entrainment more pronounced than in the standard low background diffusion case [section 4b(1)]. The entrainment zone is situated in the area of the front (at $x = -2$ km). Similar to the downwelling cases, the position and width of the entrainment zone is affected little by the presence of a highly diffusive interior. Secondary vertical zones appear behind the main entrainment zone. They are attributed to the cross-slope gradient of the vertical shear of the u field at the beginning of the stratified region. Detrainment of BBL fluid toward the interior in the presence of high background diffusion is more effective than in the standard case.

Downslope, the bottom stress is smaller than upslope but significantly larger than in the standard upwelling and highly diffusive downwelling cases. The main reason is found to be the alongslope component of the stress τ^y, which is increased. The cross-slope velocity u is not as successfully arrested as in low-background upwelling case (see also Middleton and Ramsden 1996). Interestingly, the stress upslope has a larger magnitude than in the large background diffusion downwelling case [section 4a(2)]. This is because the across-slope transport is larger upslope due to the export of downslope BBL fluid there. The upwelling high diffusivity case, as well as the case described in the following section, are the only cases found where the upslope BBL was affected by the presence of the front and the stratified lower region of the slope.

3) STEEPER BOTTOM TOPOGRAPHY

Similar to section 4a(3), the inclination of the bottom topography is increased to $\alpha = -7.2 \times 10^{-3}$ in the presence of an upwelling boundary Ekman flow.

Downslope of the front, the BML has restratified within 2 days and the temperature gradient there is larger than the interior one (Figs. 18d,h,l). Little change in the BBL stratification occurs thereafter. The cross-slope velocity is shutdown very quickly in the lower part of the boundary layer and, after the fourth day, in the upper part as well [similar to the case in section 4a(3)].

Before the front (Figs. 18b,f,j), the mixed layer height is 2 m throughout the calculations. The cross-slope velocity field exhibits strong shear above the mixed layer and is greatly reduced (to almost half) from that upslope. The alongslope profiles, too, indicate shutdown effects, a result of the intrusion of downslope flow that has already been arrested.

Below the front (Figs. 18c,g,k), the temperature profile is modified within 50 m from the bottom and bears a staircase form. The velocity field is very nearly shut down. The unusual form of the alongslope velocity between 5 and 10 m should be attributed to the mixing, which is also responsible for the temperature profile.

Again, entrainment takes place around the front, due to the divergence in the cross-slope velocity field (Fig. 19). The location of this divergence is at the front ($x = -2$ km), its intensity increased and its width reduced significantly compared to the standard upwelling case. All should be attributed to the fact that the flow below the front is arrested very quickly while the flow upslope is unchanged. Therefore, the divergence is stronger. At the same time, since the downslope flow shuts down faster, it is less able to affect wider region upslope, thus the more confined appearance of the entraining zone.

Unlike the downwelling case [section 4a(3)], the upwelling flow around the front is less effective in detraining BBL fluid toward the interior (Fig. 19). Reduction of the flow downslope, eliminates the convergence below the front that is responsible of the detrainment. Thus, there is as little tracer in the interior (shown in Romanou 1999) as in the upwelling case (Fig. 13). Moreover, little tracer escapes the stratified region and enters the upper slope since there is not enough flow to advect it upslope.

Comparing the u profiles right below the front for this simulation (Fig. 18e) to those for its downwelling counterpart (Fig. 9e), an asymmetry becomes apparent. The across-slope velocities are larger during upwelling; that is, the upslope u is greater (~ 4 cm s^{-1}) during upwelling conditions than during downwelling conditions (≈ 2.8 cm s^{-1}) even though the BBL thicknesses are the same.

This is the second time an asymmetry is induced upslope due to the presence of the front. It is believed to be due to higher entrainment of surrounding interior fluid occurring as the entraining (detraining) jet is entering (leaving) the BBL at the front. During the steeper slope conditions this “jet” is narrower than in the standard case and more entrainment of surrounding interior fluid should occur then. This would result in increased BBL transport inside the BBL upslope when entrainment conditions occur at the front (i.e., upwelling conditions downslope).

Finally, the bottom stress variability is as anticipated. The stress upslope is constant (0.13 cm^2 s^{-2}) and on the downslope is zero after 3 days. The low-stress area is almost as wide as in the standard upwelling case, but the stress is not as much reduced. Below the front, the stress is maximum because the buoyancy force increases and cannot be balanced by the Coriolis and pressure forces alone.

5. Summary and conclusions

A transport mechanism has been proposed for the convergence and detrainment of boundary layer flow in the vicinity of a temperature front that could explain features in the distribution of organic carbon and other suspended material across a sloping boundary (Lin et al. 1992; Walsh 1994; Houghton and Visbeck 1998).

A southward, steady and along-isobath interior current (deep water to the right) imposed a downwelling Ekman flow across the slope and a convergence around the front. The ensuing detrainment transported boundary layer flow away from the bottom and into the interior.

In the presence of a weakly diffusive interior, the detrainment occurred within 15 km around the front and transported boundary layer fluid to 40 m above the bottom and into the interior after 10 days. On the left side of the front, a region of intense turbulent mixing was identified. Behind the front and the detrainment zone a region of increased bottom stress was identified because the thickness of the mixed layer there increased. The front was shown to prevent the flow from continuing downslope and altered the characteristics of the upper slope significantly.

The tracer simulations agreed very well with the results of Houghton and Visbeck (1998) who injected dye tracers at the foot of a shelfbreak front. Due to convergence and detrainment, their dye tracer quickly moved into the interior and within 6 days reached 36 m above the bottom, when the cross-slope flow (u) was measured to 1 cm s^{-1}. It was shown here that the shelf break is not crucial in the convergence and export of BBL fluid. It is sufficient to have a front (without variable topography) to produce such export, based only on buoyant Ekman layer dynamics. Conversely, as it will be discussed later, the presence of a shelf break and uniform background stratification may also produce the same effect. The deformation of the front was not reported in the numerical results of Chapman and Lentz (1994), probably because their front was allowed to move freely with the freshwater inflow in their domain.

In a highly diffusive interior, the convergence region was also displaced downslope to 2 km from the front. The detrainment zone was found to be more energetic and more effective in transporting boundary layer fluid into the interior. Due to the diffusive smoothing of the velocity profiles, there was no intensive mixing area to the left of the front. The bottom stress around the front was decreased.

The presence of a steeper topography resulted in a more energetic detrainment zone that was also more confined around the front. The advection of boundary fluid away from the bottom layer was therefore more effective. Regions of intense turbulent mixing right before the front were again identified. The bottom stress was maximum below the detrainment zone.

Reversal of the interior flow direction (the upwelling Ekman flow) resulted in divergence around the front and entrainment of interior fluid into the boundary layer. The region affected by the entrainment zone is wider than before (30 km) and primarily affects the lower upslope. Buoyant Ekman boundary layer flow enters farther upslope than unstratified BBL flowed downslope in the previous case. Convective instability below the front leads to weak detrainment there so that, even in the upwelling case, a mechanism for the export of boundary layer fluid into the interior is found. The intrusion of downslope water to the left of the front resulted in significantly reduced turbulent mixing there and the position of the intensive mixing was displaced farther upslope. Below the entrainment (detrainment) zone, the bottom stress was reduced (increased).

High background diffusion and the stabilization of the boundary layer flow led to a more vigorous entrainment (detrainment) zone that was displaced farther upslope (downslope). Unlike the downwelling favorable case, intensive mixing before the front was again present. The far-upslope and far-downslope stresses were found to be more sensitive to the change in the interior diffusivity than the stress around the front.

Over a steeper slope, the entrainment of interior fluid was more effective and its width significantly less. Intensive mixing remained closer to the front than in the standard case, and the stress around the front was much reduced due to the faster arrest here.

The results presented here agree reasonably well (given the difference and dependence in z_0, the roughness scale) with measurements of the bottom stress along the U.S. east coast continental shelf (Lyne et al. 1990). On the upper slope [in all cases except high background diffusivity cases, see section 4a(2)] the drag coefficient is 8×10^{-3} cm^2 s^{-1}, while on the stratified lower slope, the shut down effects reduce the drag coefficient with values ranging from 2×10^{-3} cm^2 s^{-1} (downwelling case) to 1×10^{-3} cm^2 s^{-1} (upwelling case). Around the front the values are larger and around 15×10^{-3}–22×10^{-3} cm^2 s^{-1}.

The BBL upslope and downslope was expected to be essentially identical to the BBL seen in similar one-dimensional simulations. It was not expected that allowing a communication between the two at the front to result in the downslope BBL affecting the upslope BBL. In all but two of the cases studied this was indeed the case. However, in the high background diffusivity upwelling case, the stress and the cross-slope transport were larger due to “leakage” of slope-BBL transport across the front. It was also shown that in the steeper-slope upwelling case, the stress and cross-slope transport upslope were again increased. This time it was due to enhanced entrainment of fluid entering the upslope BBL resulting from the narrowness of the entrainment zone and increased transport into the BBL around the front.

Finally, others have previously noted on the sensitivity of the buoyant BBL predictions to the choice of background diffusivity and, not surprisingly, our results are in agreement. However, we have shown that such a sensitivity is not restricted to buoyant BBLs but apply to BBLs in general. Our results indicate that BBL stresses and transports are predominantly due to bottom-generated turbulence when the background diffusivity is low (i.e., molecular), but that they are predominantly due to background diffusivity when the diffusivity is high (order 1 cm^2 s^{-1}). Clearly, studies such as those of Polzin et al. (1997) and Ledwell et al. (1993) on interior diffusivities in the ocean have implications to BBL studies.

a. Higher resolution

The cases described in sections 4a(1) and 4b(1) were reconsidered while using higher spatial resolution; that is, $\delta x = 500$ m, $\delta y = 50$ km, and $\delta t = 1$ min. The new runs showed little change in the characteristics of the frontal dynamics as described in the basic downwelling and upwelling cases.

The position of the front changes due to inertial oscillation by three grid points (i.e., 1.5 km) in very good agreement with the coarse-resolution results. In both the downwelling and upwelling cases, tracer is ejected up to 40 m from the bottom after 10 days, while some of it has entered the stratified (neutrally stratified) region to approximately 12 km below the front in the downwelling (upwelling) case. However, the profiles of velocity and temperature around the front are not very smooth, resulting in a slightly greater bottom stress in the higher-resolution case.

b. The shelfbreak implication

The problem addressed up to this point was the BBL response to constant interior forcing over constant slope and with variable background stratification (front: Fig. 1). Extention of this work may apply to the area of the continental shelf break where a flat shelf meets the slope, that is, over variable slope and with uniform background stratification (Fig. 20).

Since in Eq. (1a) the bottom slope appears in a first-order product with the temperature field in the buoyancy term $g\beta\alpha(T - \overline{T})$, the equations of motion have the exact same form between the shelf/slope and the front experiment. In particular, in the shelf-embedded coordinate system, and on the shelf, $u_t - fv = -p_x + (A_z u_z)_z$ while again in the shelf-embedded coordinate system, on the slope, $u_t - fv = -p_x - \alpha p_z + (A_z u_z)_z$, which by hydrostacy provides,

$$u_t - fv = -p_x - g\beta\alpha(T - \overline{T}) + (A_z u_z)_z,$$

where all the terms $O(\alpha^2)$ or less are dropped. Therefore, even *without* change in the background density field, the change in the inclination of the bottom boundary provides the mechanism for similar bottom boundary layer detachment. On the shelf (where the stratification does not intersect the boundary) there are no buoyant Ekman layer effects and the flow is unchanged. On the slope, where there is temperature gradient across the slope, buoyant Ekman effects will arrest the flow.

Therefore, the shelfbreak is shown to be “equivalent” to the front, that is, an area of mean cross-slope flow convergence (divergence) and export (import) of BBL fluid toward the interior for a southerly (northerly) flowing interior current. Houghton and Visbeck (1998) did survey a shelfbreak front and found such circulation patterns. However, it is seen here that the front does not need the shelf break necessarily to force BBL detachment, the shelfbreak alone can cause the same effect. It would be interesting to use a code that permits change in the bottom topography (unlike the one used here) to look at such effects.

Acknowledgments

We thank Reinard Harkema, Jane Jimeian, and Steve Van Gorder for assisting us with the computer systems. Financial support of this work was provided by the Department of Energy (Grant DE-FG05-92ER61416) and the National Science Foundation (Grant OCE-92-06117 and OCE-9730120).

REFERENCES

Chapman D. C., and S. J. Letnz, 1994: Trapping of a coastal density front by the bottom boundary layer. *J. Phys. Oceanogr*, **24**, 1464–1479. Find this article online

Dietrich D., 1993: Sandia Ocean Modeling System. Contractor Report, Sandia National Laboratories, Albuquerque, NM, 75 pp.

Dietrich D., M. G. Marietta, and P. J. Roache, 1987: An ocean modeling system with turbulent boundary layers and topography: Numerical description. *Int. J. Numer. Methods Fluids*, **7**, 833–855. Find this article online

Ezer T., and G. L. Weatherly, 1990: A numerical study of the interaction between a deep cold jet and the bottom boundary layer of the ocean. *J. Phys. Oceanogr*, **20**, 801–815. Find this article online

Garrett C., P. McCready, and P. Rhines, 1993: Boundary mixing and arrested Ekman layers: Rotating stratified flow near a sloping boundary. *Annu. Rev. Fluid Mech*, **25**, 291–323. Find this article online

Gawarkiewicz G., and D. C. Chapman, 1992: The role of stratification in the formation and maintenance of shelfbreak fronts. *J. Phys. Oceanogr*, **22**, 753–772. Find this article online

Gregg M. C., 1989: Scaling turbulent dissipation in the thermocline. *J. Geophys. Res*, **94**, 9686–9698. Find this article online

Hogg N. G., P. Biscaye, W. Gardner, and W. J. Schmitz, 1982: On the transport and modification of Antarctic Bottom Water in the Vema Channel. *J. Mar. Res*, **40**, 231–263, (Suppl.),. Find this article online

Houghton R. W., and M. Visbeck, 1998: Upwelling and convergence in the Middle Atlantic Bight shelfbreak front. *Geophys. Res. Lett*, **25** (15,), 2765–2768. Find this article online

Killworth P. D., 1989: On the parameterization of deep convection in the ocean models. *Aha Huliko'a: Parameterization of Small Scale Processes*, P. Müller, Ed., Hawaii Institute of Geophysics, 59–74.

Ledwell J. R., A. J. Watson, and C. S. Law, 1993: Evidence for slow mixing across the pycnocline from an open-ocean tracer release experiment. *Nature*, **364** (6439,), 701–703. Find this article online

Lentz S. J., and J. H. Trowbridge, 1991: The bottom boundary layer over the northern California Shelf. *J. Phys. Oceanogr*, **21**, 1186–1201. Find this article online

Lin S., K. K. Liu, M. P. Chen, P. Chen, and F. Y. Chang, 1992: Distribution of organic carbon in the KEEP area continental margin sediments. *Terr. Atmos. Oceanic Sci*, **3**, 365–378. Find this article online

Lyne V. D., B. Butman, and W. D. Grant, 1990: Sediment movement along the U.S. east coast continental shelf—I. Estimates of bottom stress using the Grant–Madsen model and near-bottom wave and current measurements. *Contin. Shelf Res*, **10** (5,), 397–428. Find this article online

Marotzke J., 1991: Influence of convective adjustment on the stability of the thermohaline circulation. *J. Phys. Oceanogr*, **21**, 903–907. Find this article online

McCready P., and P. Rhines, 1991: Buoyant inhibition of Ekman transport on a slope and its effect on stratified spin-up. *J. Fluid Mech*, **223**, 631–661. Find this article online

McCready P., and P. Rhines, 1993: Slippery bottom boundary layers on a slope. *J. Phys. Oceanogr*, **23**, 5–22. Find this article online

Mellor G., and T. Yamada, 1982: Development of a turbulence closure model for geophysical fluid problems. *Rev. Geophys. Space Phys*, **20**, 851–875. Find this article online

Middleton J., and D. Ramsden, 1996: The evolution of the bottom boundary layer on the sloping continental shelf: A numerical study. *J. Geophys. Res*, **101** , 18061–18077, (C8),. Find this article online

Munk W. H., 1966: Abyssal recipes. *Deep-Sea Res*, **13**, 707–730. Find this article online

Polzin K. L., J. M. Toole, J. R. Ledwell, and R. W. Schmitt, 1997: Spatial variability of turbulent mixing in the abyssal ocean. *Science*, **276**, 93–96. Find this article online

Ramsden D., 1995: Response of an oceanic bottom boundary layer on a slope to interior flow. Part I: Time-independent interior flow. *J. Phys. Oceanogr*, **25**, 1672–1687. Find this article online

Romanou A., 1999: Buoyant Ekman layers over variable topography. Ph.D. dissertation, The Florida State University, 146 pp.

Trowbridge J. H., and S. J. Lentz, 1991: Asymmetric behavior of an oceanic boundary layer above a sloping bottom. *J. Phys. Oceanogr*, **21**, 1171–1185. Find this article online

Walsh J. J., 1994: Particle export at Cape Hatteras. Topical studies in oceanography. *Deep-Sea Res. II*, **41**, 603–628. Find this article online

Weatherly G. L., and P. J. Martin, 1978: On the structure and dynamics of the oceanic bottom boundary layer. *J. Phys. Oceanogr*, **8**, 557–570. Find this article online

Weatherly G. L., and E. A. Kelley, 1985: Two views of the cold filament. *J. Phys. Oceanogr*, **15**, 68–61. Find this article online

Yamada T., 1979: An application of a three-dimensional, simplified second-moment closure numerical model to study atmospheric effects of a large cooling-pond. *Atmos. Environ*, **13**, 693–704. Find this article online

Yin F. L., and E. S. Sarachik, 1994: An efficient convective adjustment scheme for ocean general circulation models. *J. Phys. Oceanogr*, **24**, 1425–1431. Find this article online

---

Figures

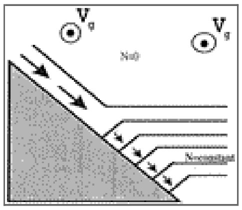

Click on thumbnail for full-sized image.

FIG. 1. Schematic representation of the downwelling case. Boundary layer formed over bottom with constant slope and varying interior stratification. The interior current V_g flows southward and the Coriolis parameter f is positive. The temperature jump above the BBL in the neutrally stratified region limits the BBL thickening and is similar to the BBL over a level bottom while the BBL in the stratified region is a buoyant BBL

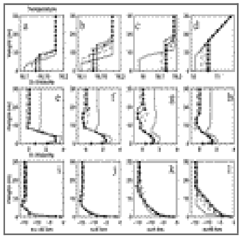

Click on thumbnail for full-sized image.

FIG. 2. Downwelling case: Vertical profiles *upslope* (first column), *before* the front (second column), *after* the front (third column), and *downslope* (last column) of temperature (°C), cross-slope velocity u (cm s^{-1}), and alongslope velocity v (cm s^{-1}) at days 2 (continuous line), 4 (dashed line), 6 (dashed dotted line), 8 (continuous dotted line), and 10 (continuous crossed line). Labels at the bottom of each column indicate the cross-slope displacement relative to the initial position of the front. Due to the "inertial shift," the front is located at x = 2 km

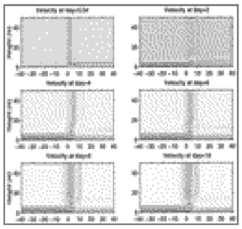

Click on thumbnail for full-sized image.

FIG. 3. Downwelling case: Cross-slope sections of the (u, w) velocity (cm s^{-1}) at different time steps. The vertical axis is perpendicular to the bottom slope and denotes height above the bottom. The horizontal axis points downslope and denotes the distance relative to the initial position of the front. Due to the "inertial shift," the front is now located at x = 2 km

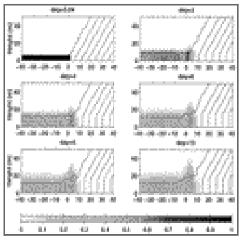

Click on thumbnail for full-sized image.

FIG. 4. Downwelling case: Passive tracer and temperature (°C) sections across the bottom boundary. Isotherm contour interval = 1°C, max temperature = 16.18°C. The front is located at x = 2 km

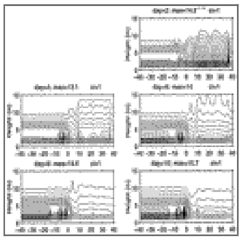

Click on thumbnail for full-sized image.

FIG. 5. Downwelling case: Across-slope sections of the vertical momentum (eddy) diffusivity (cm^{2} s^{-1}). The maximum values are indicated for each day and the contour interval is 1 cm^{2} s^{-1}. The vertical axis is perpendicular to the bottom slope and denotes height above the bottom. The horizontal axis points downslope and denotes the distance relative to the initial position of the front. The front is located at x = 2 km

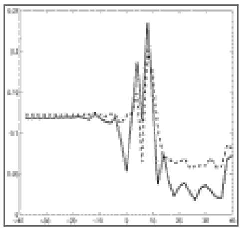

Click on thumbnail for full-sized image.

FIG. 6. Downwelling case: Bottom stress (in cm^{2} s^{-2}) across the bottom boundary at day 5 (dashed line) and day 10 (continuous line). The horizontal axis is the distance downslope from the front located at x = 2 km

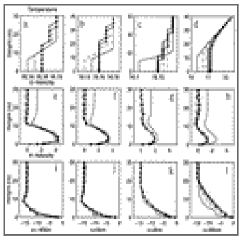

Click on thumbnail for full-sized image.

FIG. 7. Highly diffusive interior downwelling case: As in Fig. 2, vertical profiles *upslope* (first column), *before* the front (second column), *after* the front (third column), and d*ownslope* (last column) of temperature (°C), cross-slope velocity u (cm s^{-1}) and alongslope velocity υ (cm s^{-1}) at different times. Due to the "inertial shift," the front is located at x = 2 km

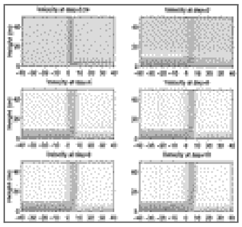

Click on thumbnail for full-sized image.

FIG. 8. Highly diffusive interior downwelling case: As in Fig. 3, cross-slope sections of the (u, w) velocity (cm s^{-1}) at different time steps. Due to the "inertial shift," the front is now located at x = 2 km

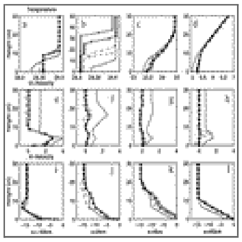

Click on thumbnail for full-sized image.

FIG. 9. Steeper slope downwelling case: As in Fig. 2, vertical profiles *upslope* (first column), *before* the front (second column), *after* the front (third column), and *downslope* (last column) of temperature (°C), cross-slope velocity u (cm s^{-1}) and along-slope velocity υ (cm s^{-1}) at different times. Due to the "inertial shift," the front is located at x = 2 km

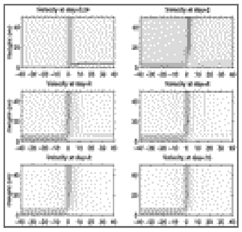

Click on thumbnail for full-sized image.

FIG. 10. Steeper slope downwelling case: As in Fig. 3, cross-slope sections of the (u, w) velocity (cm s^{-1}) at different time steps. Due to the "inertial shift," the front is now located at x = 2 km

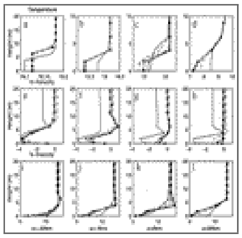

Click on thumbnail for full-sized image.

FIG. 11. Upwelling case: As in Fig. 2, vertical profiles *upslope* (first column), *before* the front (second column), *after* the front (third column), and *downslope* (last column) of temperature (°C), cross-slope velocity u (cm s^{-1}) and alongslope velocity υ (cm s^{-1}) at different times. Due to the "inertial shift" of the front, the shelf edge is located at x = −2 km

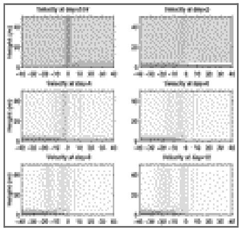

Click on thumbnail for full-sized image.

FIG. 12. Upwelling case: As in Fig. 3, cross-slope sections of the (u, w) velocity (cm s^{-1}) at different time steps. The shelf edge is located at $x = -2$ km

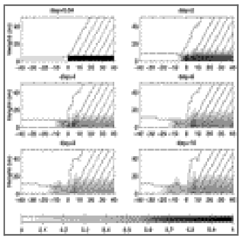

Click on thumbnail for full-sized image.

FIG. 13. Upwelling case: As in Fig. 4, passive tracer and temperature (°C) sections across the bottom boundary. The front is located at $x = 2$ km

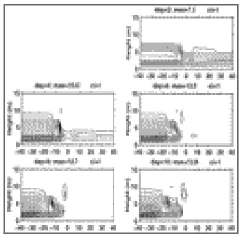

Click on thumbnail for full-sized image.

FIG. 14. Upwelling case: As in Fig. 5, cross-slope sections of the vertical momentum (eddy) diffusivity (cm^2 s^{-1}). The front is located at $x = -2$ km

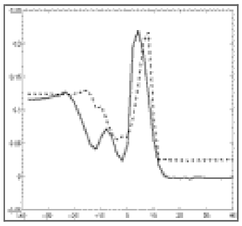

Click on thumbnail for full-sized image.

FIG. 15. Upwelling case: As in Fig. 6, bottom stress (in cm^2 s^{-2}) across the bottom boundary, at day 5 (dashed line) and day 10 (continuous line). Front at $x = -2$ km

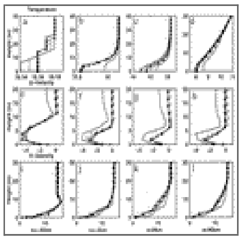

Click on thumbnail for full-sized image.

FIG. 16. Highly diffusive interior upwelling case: As in Figs. 2 and 11, vertical profiles *upslope* (first column), *before* the front (second column), *after* the front (third column), and *downslope* (last column) of temperature (°C), cross-slope velocity u (cm s^{-1}) and alongslope velocity v (cm s^{-1}) at different times. Due to the "inertial shift," the front is located at $x = -2$ km

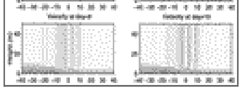

Click on thumbnail for full-sized image.

FIG. 17. Highly diffusive interior upwelling case: As in Figs. 3 and 12, cross-slope sections of the (u, w) velocity (cm s^{-1}) at different time steps. Due to the "inertial shift," the front is now located at $x = -2$ km

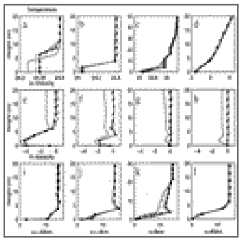

Click on thumbnail for full-sized image.

FIG. 18. Steeper slope upwelling case: As in Fig. 2, vertical profiles *upslope* (first column), *before* the front (second column), *after* the front (third column), and *downslope* (last column) of temperature (°C), cross-slope velocity u (cm s^{-1}) and alongslope velocity v (cm s^{-1}) at different times. Due to the "inertial shift," the front is located at $x = -2$ km

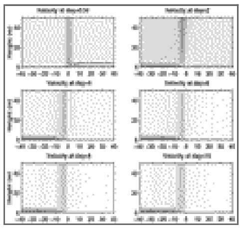

Click on thumbnail for full-sized image.

FIG. 19. Steeper slope upwelling case: The front is located at $x = -2$ km

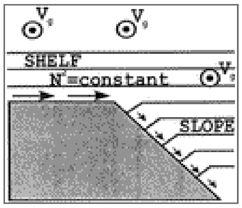

Click on thumbnail for full-sized image.

FIG. 20. Schematic representation of the downwelling case near the shelf break: Ekman flow (arrows) over boundary with variable slope and constant stratification N^2. The interior current V_g flows southward and the Coriolis parameter f is positive. Over the shelf, which is assumed level, the only effect of N^2 = const is to limit the thickness of the bottom boundary layer. Otherwise, the BBL stress and transport are as for a BBL formed in a $N^2 = 0$ case (Weatherly and Martin 1978). Over the slope, when the bottom slope is assumed fixed, the BBL is a buoyant one as described in Middleton and Ramsden (1996)

Corresponding author address: Dr. Anastasia Romanou, RSMAS/MPO, University of Miami, 4600 Rickenbacker Cswy., Miami, FL 33149. E-mail: aromanou@rsmas.miami.edu

top

© 2008 American Meteorological Society Privacy Policy and Disclaimer
Headquarters: 45 Beacon Street Boston, MA 02108-3693
DC Office: 1120 G Street, NW, Suite 800 Washington DC, 20005-3826
amsinfo@ametsoc.org Phone: 617-227-2425 Fax: 617-742-8718
Allen Press, Inc. assists in the online publication of *AMS* journals.